Materials Today Communications 51 (2026) 114808

Contents lists available at ScienceDirect

Materials Today Communications

journal homepage: www.elsevier.com/locate/mtcomm

Microstructured cellulose acetate biointerfaces regulate mesenchymal stem cell response and promote osteogenic commitment

Eleni Kanakousaki [a,b], Paraskevi Kavatzikidou [b], Panagiotis Daskalakis [b,c], Konstantina Alexaki [b], Stella Maragkaki [b], Alexandra Manousaki [b], Jagrati Dwivedi [d], George Kenanakis [b], Thomas F. Keller [d,e], Emmanuel Stratakis [b,f,*], Anthi Ranella [b,**]

[a] Department of Biology, University of Crete, Heraklion, Crete 70013, Greece
[b] Institute of Electronic Structure and Laser, Foundation for Research and Technology – Hellas (FORTH), Heraklion, Crete 70013, Greece
[c] School of Medicine, University of Crete, Heraklion, Crete 70013, Greece
[d] Centre for X-ray and Nano Science CXNS, Deutsches Elektronen-Synchrotron DESY, Hamburg D-22603, Germany
[e] Department of Physics, University of Hamburg, Hamburg D-22607, Germany
[f] Department of Physics, University of Crete, Heraklion, Crete 70013, Greece

ARTICLE INFO

Keywords:
Cellulose acetate
Soft lithography
Microtopography
Interfacial mechanics
Mechanical cues
Mesenchymal stem cells
Osteogenic commitment

ABSTRACT

Cellulose acetate (CA) is an attractive and sustainable biopolymer for biomedical applications due to its biocompatibility, tunable physicochemical properties, and compatibility with microfabrication. Mechanical stimuli such as topographical cues are known to profoundly influence stem cell behavior, yet their employment in cellulose acetate systems remains underexplored. In this study, we present a reproducible soft-lithography approach to engineer CA scaffolds with well-defined microstructured topographies and controlled surface roughness. The interfacial characteristics of the resulting biointerfaces were assessed using atomic force microscopy. Mesenchymal stem cells cultured on these microstructured platforms exhibited enhanced adhesion, cytoskeletal organization, and focal adhesion formation compared with flat CA controls. Notably, surfaces with intermediate roughness modulated the nuclear translocation of the mechanosensitive regulator TAZ, relative to flat and high roughness surfaces, in a topography dependent manner, suggesting activation of adhesive and cytoskeletal signaling pathways. Under osteogenic conditions, these biointerfaces further supported elevated alkaline phosphatase activity and osteopontin expression, indicative of enhanced early osteogenic commitment. Overall, this work demonstrates that microstructured CA biointerfaces act as instructive platforms that modulate mesenchymal stem cell response through topography-mediated mechanical cues, highlighting their potential as sustainable platforms for bone tissue engineering applications.

1. Introduction

Bone disorders, caused by injury, tumor resection, ageing, or diseases like osteoporosis and arthritis, pose significant health and economic challenges worldwide [1,2]. Treatment costs are high, compounded by long healing times. While bone possesses a remarkable regenerative capacity, large or complex defects often fail to heal properly [1,3,4]. Current therapeutic options, including autografts and allografts, are limited by donor site morbidity, immune rejection, and risks of disease transmission [4]. Consequently, Bone Tissue Engineering (BTE) has emerged as a promising alternative, aiming to enhance the innate regenerative potential through engineered scaffolds and cell-based therapies. Therefore, research in BTE focuses on stem cells, such as mesenchymal stem cells (MSCs), and how to influence their response through environmental cues [2].

Cells are mechanosensitive, responding to diverse physical stimuli, such as substrate topography, stiffness, and shear stress. They can convert physical stimuli into biochemical signals through mechanotransduction, where cytoskeletal-mediated forces, exerted by the properties of the adhering substrates, are transmitted into the nucleus, inducing functional changes [5,6]. Micro- and nano-scale surface features guide stem cells' adhesion, migration, differentiation, and specific

* Corresponding author at: Institute of Electronic Structure and Laser, Foundation for Research and Technology – Hellas (FORTH), Heraklion, Crete 70013, Greece
** Corresponding author.
E-mail addresses: stratak@iesl.forth.gr (E. Stratakis), ranthi@iesl.forth.gr (A. Ranella).

https://doi.org/10.1016/j.mtcomm.2026.114808
Received 1 December 2025; Received in revised form 3 February 2026; Accepted 5 February 2026
Available online 6 February 2026

gene expression, emphasizing the importance of mimicking the extracellular matrix (ECM) environment in scaffold design. Despite significant advances, the detailed mechanisms underlying these responses remain unclear [3,7,8].

Substrate properties, such as stiffness and roughness, may regulate MSCs' response through mechanosensitive signalling pathways [9–11]. Mechanical forces are transmitted through the cytoskeleton, notably through actin stress fibers, ultimately affecting cell shape and function [12,13]. Cell shape influences differentiation [14], with cytoskeletal remodelling influencing key transcriptional regulators like YAP/TAZ [15]. YAP/TAZ are key regulators of MSCs' mechanotransduction, driving anti-apoptosis, proliferation, gene expression and differentiation [16,17]. Several osteogenic genes (*e.g.,* Runx2, ALP) appear to interact with YAP/TAZ, indicating the association of mechanotransduction to bone formation [9,18–21].

Surface topography significantly affects cell morphology, spreading, and orientation through contact guidance, wherein cells orient along topographical features [14,22]. Cells can sense such surface patterns ranging from 10 nm to 100 μm with various structures, such as gratings, wrinkles, pillars, spikes and particles, capable of modulating cell behavior. Topographical characteristics have been reported to regulate MSCs' osteogenic differentiation [6,23–28]. Surface topography promotes integrin activation, focal adhesion (FA) formation (*e.g.,* Vinculin, Paxillin) and cytoskeletal alignment, providing structural support and function [6,29]. Integrins are involved in cell-matrix adhesion through FAs, linking the ECM to the cytoskeleton, mediating cell adhesion, migration and signaling [30,31], while force-sensitive proteins regulate actomyosin contractility, during FA maturation, influencing downstream cellular functions [32]. Recent reviews have further highlighted the central role of scaffold material properties and microtopographical cues in regulating stem cell fate and osteogenic outcomes in BTE [33–35].

Soft lithography is a widely used non-photolithographic technique, based on self-assembly and replica molding, for creating high-resolution micro- and nano-structures. It appears as a non-toxic, effective, inexpensive, and high-throughput method [36–38]. Although an initial master fabrication step (*e.g.,* photolithography, e-beam lithography) is required, it is performed only once [38]. Soft lithography typically involves an elastomeric poly(dimethylsiloxane) (PDMS) stamp for transferring patterns with feature sizes ranging from 30 to 100 μm [36,37].

Among natural polymers, cellulose stands out for its abundance, eco-friendliness, and excellent mechanical properties. Cellulose acetate (CA) is the most valuable cellulose derivative due to its biocompatibility, biodegradability, low cost, and excellent mechanical and chemical stability. CA exists as cellulose triacetate and diacetate, depending on the degree of acetate substitution, and is typically soluble in organic solvents like acetone and dioxane [39–41]. CA has gained significant attention in biomedicine, particularly for applications in drug delivery, tissue engineering, and sutures, due to its favorable properties [42]. However, although mechanical stimuli such as topographical cues profoundly influence stem cell responses, their employment in cellulose acetate systems remains underexplored.

Biomaterials substrates with well-defined topographies offer a promising strategy to modulate cellular responses by inducing specific biochemical signals according to therapeutic needs [27,43]. This study aims to explore the influence of micropatterned CA biointerfaces on MSCs' response and early osteogenic commitment. Microstructured CA replicas with low and high roughness features were fabricated *via* soft lithography, and their effects on MSCs adhesion, proliferation, interfacial mechanics (*via* focal adhesions and TAZ localization), and early-to-middle osteogenic differentiation were investigated. The advantages of soft lithography were leveraged to fabricate polymeric micropatterned surfaces in a repeatable manner, and their morphological, physicochemical and mechanical characteristics were assessed. We hypothesized that CA microtopographies modulate MSC behavior by altering interfacial mechanics at the cell–material interface, thereby regulating focal adhesion maturation and YAP/TAZ-dependent mechanotransduction. Specifically, we anticipated that LR would provide optimal mechanical cues for early osteogenic commitment. Overall, this work aims to elucidate how microstructured CA biointerfaces regulate MSC mechanotransduction and osteogenic signaling, supporting the development of sustainable polymeric scaffolds for BTE applications.

2. Materials and methods

2.1. Preparation of the scaffolds

2.1.1. Fabrication of laser micro-structured substrates and PDMS negative molds

Silicon substrates and the PDMS (SYLGARD 184, Dow Corning, Midland, MI, USA) negative molds were fabricated as reported previously [44–47] and they were used for the reproduction of the initial Si morphologies by producing CA scaffolds. The ultra-fast laser-fabricated Si substrate is characterized as the "master" substrate. An adequate number of PDMS negative molds were produced for flat, low (LR) and high roughness (HR) topographies, with an overall spike area of 0.5 cm^2 (Supplementary Fig. 1(A)).

2.1.2. Fabrication of CA replicas via soft lithography

Using the PDMS negative mold (negative spikes morphology), CA replicas were produced, as they reproduce the surface topography of the original Si masters. Polymeric solutions of 8 % (w/w), 10 % (w/w), 15 % (w/w), 30 % (w/w) and 40 % (w/w) CA (Mn~30,000 g/mol, Sigma-Aldrich, Saint Louis, MO, USA) (acetyl content: 39.3–40.3 wt%, corresponding to cellulose diacetate) in acetone (≥99.5 %, Honeywell, Charlotte, NC, USA) were carefully prepared by heating the mixture at 50 °C for 20 min. Then, the solutions were stirred (700–800 rpm for 40 min at 50 °C). A droplet (60 μL/PDMS mold) of CA solution was poured on each PDMS negative mold. The deposited CA droplet was allowed to rest for 2 min and then a 13 mm diameter glass coverslip (VWR, Avantor Inc., Radnor, PA, USA) was gently placed on top of the droplet, without applying external pressure. This step facilitated handling and enabled easier peeling of the replicas after complete drying. Following the evaporation of the solvent, the CA-coated PDMS mold was heated on a heating plate at 50 °C for 3 h. Then, the CA replicas were peeled from the PDMS negative mold (Supplementary Fig. 1**(B)**). Throughout the manuscript, the term "CA replicas" is used when referring to the fabricated substrates/replicas in the context of material preparation and physicochemical characterization, while the term "CA biointerfaces" is used when referring to the same substrates in the context of cell–material interactions and biological studies.

2.2. Characterization of CA replicas

2.2.1. Scanning electron microscopy

CA replicas were analyzed by Scanning Electron Microscopy (SEM). The samples were sputter-coated with a 15 nm film of Au (BAL-TEC SCD 050) (Balzers, Liechtenstein) before SEM examination. The SEM used for the acquisition of the images was the JEOL JSM-6390 LV or JSM-IT700HR (JEOL Ltd., Tokyo, Japan). SEM images were analyzed using ImageJ software (version 2.16.0/1.54p, National Institutes of Health, Bethesda, MD, USA) to calculate CA replica feature height and width, based on measurements from multiple regions per sample (Supplementary Table 1).

2.2.2. In vitro degradation and swelling assay

Freshly prepared CA replicas were fully dried (as described in 2.1.2.) and weighed to obtain the initial weight (W_o). The samples were then immersed in phosphate-buffered saline (PBS, pH 7.4) (Sigma-Aldrich, Saint Louis, MO, USA) at 37 °C. At predetermined time intervals, samples were removed, dried, and weighed (Wt). Independent samples were used for each time point to minimize handling. The time intervals

examined were $t = 0$, 2, 7, 14, 21 and 40 days. The weight loss of the scaffolds was calculated according to Eq. (1):

$$\textit{Weight loss}\ (\%) = \frac{W_0 - W_t}{W_0} \times 100 \quad (1)$$

For the swelling assay, the dried scaffolds were first weighed (initial weight, W_0) and then immersed in PBS (pH 7.4) at 37 °C. The swelling kinetics were investigated by the gravimetric method. At predetermined time intervals, the samples were removed from PBS, wiped dry with filter paper on the surface, and weighed. The time intervals examined were $t = 20$, 50, 80, 100, 120, 160, 220, 300 and 380 min. The swelling ratio at time t was calculated using the Eq. (2):

$$\textit{Swelling ratio}\ (\%) = \frac{W_t - W_0}{W_0} \times 100 \quad (2)$$

Both degradation and swelling assays were performed in triplicate (n = 3).

2.2.3. Wettability

The wettability of the flat and patterned CA replicas was evaluated using an optical contact angle system (OCA 15EC, DataPhysics Instruments GmbH, Filderstadt, Germany) with the sessile drop method. A 4 μL droplet of distilled–deionized water was gently deposited onto each surface using a micro-syringe, and images were recorded using the integrated CCD camera. Contact angles were automatically calculated using the instrument's software (SCA-20).

2.2.4. UV-Vis spectroscopy

The optical properties of the flat and patterned CA substrates were characterized using a Horiba Duetta™ (Horiba, Ltd., Kyoto, Japan) UV-Vis Spectrophotometer. Prior to analysis, each scaffold was carefully secured in the spectrophotometer's sample holder. Absorbance and transmittance spectra were collected across a wavelength range of 250–1000 nm, with a 2 nm step size. The acquired data were analyzed using OriginPro 2016 Data Analysis and Graphing Software (OriginLab Corporation, Northampton, MA, USA).

2.2.5. Fourier transform infrared (FT-IR) analysis

The chemical composition of the flat and patterned CA replicas were analyzed using FT-IR spectroscopy and characteristic peaks corresponding to CA were identified to confirm the composition of the samples; FT-IR (absorbance) experiments were carried out with a Bruker Vertex 70 v FT-IR vacuum spectrometer (Bruker Optics GmbH, Ettlingen, Germany) equipped with a A225/Q Platinum Attenuated Total Reflectance (ATR) unit with single reflection diamond crystal through total reflection measurements, in a spectral range of 3200–350 cm^{-1}. A broad band KBr beamsplitter and a room temperature broad band triglycine sulfate (DTGS) detector were used, while interferograms were collected at 4 cm^{-1} resolution (8 scans), apodized with a Blackman-Harris function, and Fourier transformed with two levels of zero filling to yield spectra encoded at 2 cm^{-1} intervals. Before scanning the samples, a background diamond crystal was recorded, and each sample spectrum was obtained by automatic subtraction of it. Spectral acquisition and baseline correction were performed using the OPUS 8.9 software package (Bruker Optics GmbH, Ettlingen, Germany). Additional data processing and plotting were carried out using OriginPro 2016 Data Analysis and Graphing Software (OriginLab Corporation, Northampton, MA, USA).

2.2.6. Atomic force microscopy

2D topographic and phase images and force distance curves were obtained with a Dimension Icon Atomic Force Microscope (AFM) instrument equipped with a Nanoscope controller V (both Bruker, Billerica, MA, USA) in peak force mode [48]. Scan ranges varied from 50 μm to 0.5 μm at typical, adjusted scan rates of 0.2–1 Hz and image resolution of 256 × 256 pixels up to 512 × 512 pixels. RTESPA-300 etched silicon probes with a reflective Al coating, and a nominal resonance frequency of 300 kHz were used. The cantilever stiffness was calibrated on a sapphire reference sample, and a deflection sensitivity of 86.5 nm/V and a spring constant of 20.75 N/m were obtained. The tip radius was determined on a rough Ti sample to be 16.5 nm, corresponding to a penetration depth of 6 nm. The software NanoScope Analysis 3.00 (Bruker, Billerica, MA, USA) was used for the AFM data analysis. A plane fit algorithm was applied to the topographic height images to correct for any possible macroscopic sample tilts. Parts of the images, largely from the rough surfaces, were masked to consider only areas relevant for the plane surface. The retraction part of the force curves was fitted by including the adhesion force based on the Derjaguin, Muller, and Toporov (DMT) model, assuming a spherical indenter for small indentations and tip–sample adhesion [49–51]. The adhesion force was manually adjusted to the minimum of the force curve, and fit boundaries were set to 90 % and 0 % to reliably obtain the reduced Young's modulus and the R^2 for the quality of fit for each of the samples. For statistics, at least 3 force curves were analyzed, and the resulting reduced Young's modulus was averaged to obtain the mean value for the given sample.

2.3. Cell studies

2.3.1. Cell cultures

Mouse bone marrow MSCs (C57BL/6, Cyagen, Santa Clara, CA, USA) were used for all experiments. Cells were cultured in Dulbecco's modified Eagle's medium (DMEM) low glucose (1000 mg/L glucose; Gibco™, Waltham, MA, USA), supplemented with 10 % fetal bovine serum (FBS; Gibco™, Waltham, MA, USA) and 1 % penicillin/streptomycin (PS; Gibco™, Waltham, MA, USA). Cultures were maintained at 37 °C in a humidified 5 % CO_2 incubator, with medium changes every 3–4 days. MSCs between passages 5–10 were used. CA replicas were UV-sterilized (λ = 254 nm, 30 min) in a cell culture hood and placed in sterile 24- or 48-well plates (Corning Inc., New York, NY, USA). A cell suspension of 30,000 cells/mL was seeded onto the scaffolds for short-term (1, 3 days) and long-term (8, 15, 22 days) studies. Tissue culture plastic (TCP) coverslips (polystyrene, Corning Inc., New York, NY, USA) were used as controls.

2.3.2. Scanning electron microscopic analysis of MSCs on the CA scaffolds

MSCs cultured on the patterned CA replicas were examined by scanning electron microscopy (SEM) using a JEOL JSM-6390 LV or JSM-IT700HR (JEOL Ltd., Tokyo, Japan). After culture termination, samples were rinsed twice with 0.1 M sodium cacodylate buffer (SCB; Sigma-Aldrich, Saint Louis, MO, USA), pH 7.4) for 5 min at 4 °C and fixed in 2.5 % glutaraldehyde (Sigma-Aldrich, Saint Louis, MO, USA) / 2.5 % paraformaldehyde (PFA; Sigma-Aldrich, Saint Louis, MO, USA) in SCB for 30 min at 4 °C. Samples were then washed twice with SCB and dehydrated through a graded ethanol series (30 %, 50 %, 70 %, 90 %, 100 %), 10 min each at 4 °C. Following dehydration, samples were immersed in HMDS (Sigma-Aldrich, Saint Louis, MO, USA)/ethanol (Sigma-Aldrich, Saint Louis, MO, USA) (50:50) for 30 min and 20 min, and finally in 100 % HMDS for 20 min twice, then left to dry overnight. Prior to imaging, samples were sputter-coated with a 15 nm gold layer (Baltec SCD 050, BAL-TEC AG, Liechtenstein).

2.3.3. Live/dead assay

Cell viability was assessed using the LIVE/DEAD™ Viability/Cytotoxicity Assay Kit (L3224, Thermo Scientific, Waltham, MA, USA). MSCs (30,000 cells/mL) were seeded onto the CA replicas and incubated for 24 h under standard culture conditions. After medium removal, samples were washed twice with PBS. A working Live/Dead solution was prepared by adding 20 μL of 2 mM ethidium homodimer-1 (EthD-1) to 10 mL PBS (final concentration 4 μM), followed by the addition of 5 μL of 4 mM calcein-AM stock (final concentration 2 μM). A volume of 500 μL of this solution was added to each sample and incubated for

45 min at room temperature. Samples were then washed once with PBS, and fluorescence images were acquired using a Carl Zeiss (ZEISS, Oberkochen, Germany) fluorescence microscope, with a 10x objective lens.

2.3.4. Osteogenic differentiation

To induce osteogenic differentiation, 24 h after MSCs seeding, the standard culture medium was replaced with the osteogenic medium. The osteogenic medium (OSTEO) consisted of DMEM - high glucose (4500 mg/L glucose) (Gibco™, Waltham, MA, USA), 10 % FBS, 1 % penicillin/streptomycin (PS), 0.1 mM dexamethasone (Sigma-Aldrich, Saint Louis, MO, USA), 0.17 mM L-ascorbic acid and 10 mM β-glycerophosphate (Sigma-Aldrich, Saint Louis, MO, USA). The OSTEO medium was renewed every three days, and the differentiation was assessed at 1 + 7 days, 1 + 14 and 1 + 21 days. For comparison purposes, samples without OSTEO medium were also studied at time points 8, 15 and 22 days.

2.3.5. Immunocytochemical assay

For immunocytochemistry, samples were washed twice with PBS (pH 7.4) and fixed with 4 % paraformaldehyde (PFA) for 15 min at room temperature. After two additional PBS washes, cells were permeabilized with 0.1 % Triton X-100 (Sigma-Aldrich, Saint Louis, MO, USA) for 5 min, washed again, and blocked with 2 % bovine serum albumin (BSA) (Sigma-Aldrich, Saint Louis, MO, USA) in PBS for 30 min. Cells were then incubated with the primary antibodies (Table 1) overnight at 4 °C. The following day, samples were washed and incubated with the corresponding secondary antibodies (Table 1) and phalloidin for 2 h, followed by nuclear staining with 4',6-diamidino-2-phenylindole (DAPI) (Invitrogen™, Waltham, MA, USA). Imaging was performed using a Leica SP8 laser scanning confocal microscope (Leica Microsystems, Wetzlar, Germany).

2.4. Image analysis

Image processing was performed using ImageJ software (version 2.16.0/1.54p, National Institutes of Health, Bethesda, MD, USA) [52] and CellProfiler 4.2.8 software (Broad Institute, Cambridge, MA, USA). CellProfiler was used to characterize the cell morphological parameters: nuclear aspect ratio and nuclear to cytoplasmic protein intensities. Different image processing pipelines were generated to load 2- or 3-channel immunofluorescent images for each analysis. This was followed by automated detection of cell nuclei, cell and nuclear aspect ratio and nuclear to cytoplasmic ratios of the protein TAZ [53–55]. Wherever applicable, mean fluorescence intensity was evaluated across multiple independent samples and multiple fields of view per condition, using identical acquisition and analysis parameters, to ensure consistency and reproducibility of the observed trends. Cell proliferation was assessed by automated nuclear counting from fluorescence images using ImageJ, based on DAPI-stained nuclei, across multiple fields of view per sample.

Table 1
Antibodies used for this investigation. All antibodies were diluted in 1 % BSA in PBS 1x solution, at the respective concentrations.

First Antibody	Second Antibody
Paxillin (rabbit) (Abcam, UK) (1:400)	Goat anti-rabbit 555 (Biotium Inc., Fremont, CA, USA) (1:600)
Osteopontin (rabbit) (Abcam, UK) (1:500)	Goat anti-rabbit IgG 647 (Biotium Inc., Fremont, CA, USA) (1:500)
TAZ (rabbit) (Cell Signaling Technology, Danvers, MA, USA) (1:300)	Goat anti-rabbit IgG 647 (Biotium Inc., Fremont, CA, USA) (1:500)
ALP (rabbit) (Abcam, UK) (1:400)	Goat anti-rabbit 555 (Biotium Inc., Fremont, CA, USA) (1:600)
Phalloidins	
Actin Phalloidin 568 (Biotium Inc., Fremont, CA, USA) (1:500) or 680 (Biotium Inc., Fremont, CA, USA) (1:800) or TRITC 532 (Millipore, Burlington, MA, USA) (1:1000)	

2.5. Statistical analysis

The data were subjected to one-way ANOVA followed by post hoc Tukey HSD for multiple comparisons between pairs of means with the software GraphPad Prism 8.0.2 (Dotmatics, United Kingdom). The statistically significant difference between experimental results was indicated by $*p \leq 0.05$, $**p \leq 0.01$, $***p \leq 0.001$, $****p \leq 0.0001$. The error bars denote the standard deviation of the mean. Unless otherwise specified, all experiments were performed with a minimum of three independent replicates.

3. Results & discussion

3.1. Scaffold fabrication, physicochemical and surface-mechanical characterization

Fabrication of CA replicas. Five different concentrations of CA in acetone (8 % (w/w), 10 % (w/w), 15 % (w/w), 30 % (w/w) and 40 % (w/w)) were prepared to find out which CA concentration was ideal. The produced CA solutions were then cast on the PDMS negative molds to form patterned substrates. From now on, the 8 %, 10 %, 15 %, 30 % and 40 % CA replicas will be called 8CA, 10CA, 15CA, 30CA and 40CA replicas, respectively.

Due to the low polymer content in 8CA replicas, the resulting surfaces were very fragile and were torn when they were peeled from the PDMS negative mold (Supplementary Fig. 2(A)). At higher CA concentrations, the replicas exhibited holes caused by rapid solvent evaporation (Supplementary Figs. 2 (C) and (E)). Moreover, CA solutions above 20 %-30 % became difficult to handle due to high viscosity, while the produced replicas were excessively thick and non-uniform (thick central region: ~3 mm and thinner edges: ~1 mm). The best results were obtained using 10CA and 15CA solutions. SEM images (Supplementary Fig. 3) showed that both sample types were intact, defect-free surfaces of optimal thickness. While 8CA, 30CA, and 40CA replicas were well replicated (Supplementary Figs. 2(B), (D), (F)), they were not ideal due to fragility, difficult handling and significant loss of surface area (Supplementary Figs. 2(A), (C), (E)).

10CA provided optimal surface integrity and topographical fidelity without defects or excessive thickness. Therefore, this concentration was used for subsequent scaffold fabrication and biological evaluation. Although low concentrations of CA are optimal for soft lithography, Daskalakis et al. [56] demonstrated that a concentration of approximately 30 % CA is ideal for 3D bioprinting. These findings highlight the versatility of CA across different fabrication techniques.

Structural characterization of CA replicas. As shown in Fig. 1**(A)**, the flat samples exhibited smooth surfaces with no spikes, while the LR and HR topographies were distinguished by spike height, with HR biointerfaces (Fig. 1**(C)**) displaying sharper and more defined peaks. In addition, no significant differences were observed between the three CA samples and their original Si masters [44–47].

The geometrical characteristics of the Si masters were previously measured [44–47]. In these studies, poly(lactide-co-glycolide) (PLGA) was used to fabricate patterned surfaces *via* soft lithography, using the same PDMS negative molds. It was found that the spikes of LR topographies had a height of 3.06 ± 0.40 μm and a width of 2.93 ± 0.30 μm, whereas the spikes of HR topographies had a height of 10.55 ± 1.10 μm and a width of 4.68 ± 0.41 μm [43,44]. In the case of CA biointerfaces, the spikes of LR topographies had a height of 2.43 ± 0.19 μm and a width of 1.70 ± 0.23 μm, whereas the spikes of HR topographies had a height of 9.19 ± 0.66 μm and a width of 5.03 ± 0.8 μm (Supplementary Table 1). Similar measurements exist for PCL biointerfaces (unpublished data). Although minor variations in spike dimensions were noted between polymeric materials and Si masters, they fell within the standard deviation range. This suggests that soft lithography offers high replication fidelity, accurately transferring micropatterned topographies on biodegradable polymers.

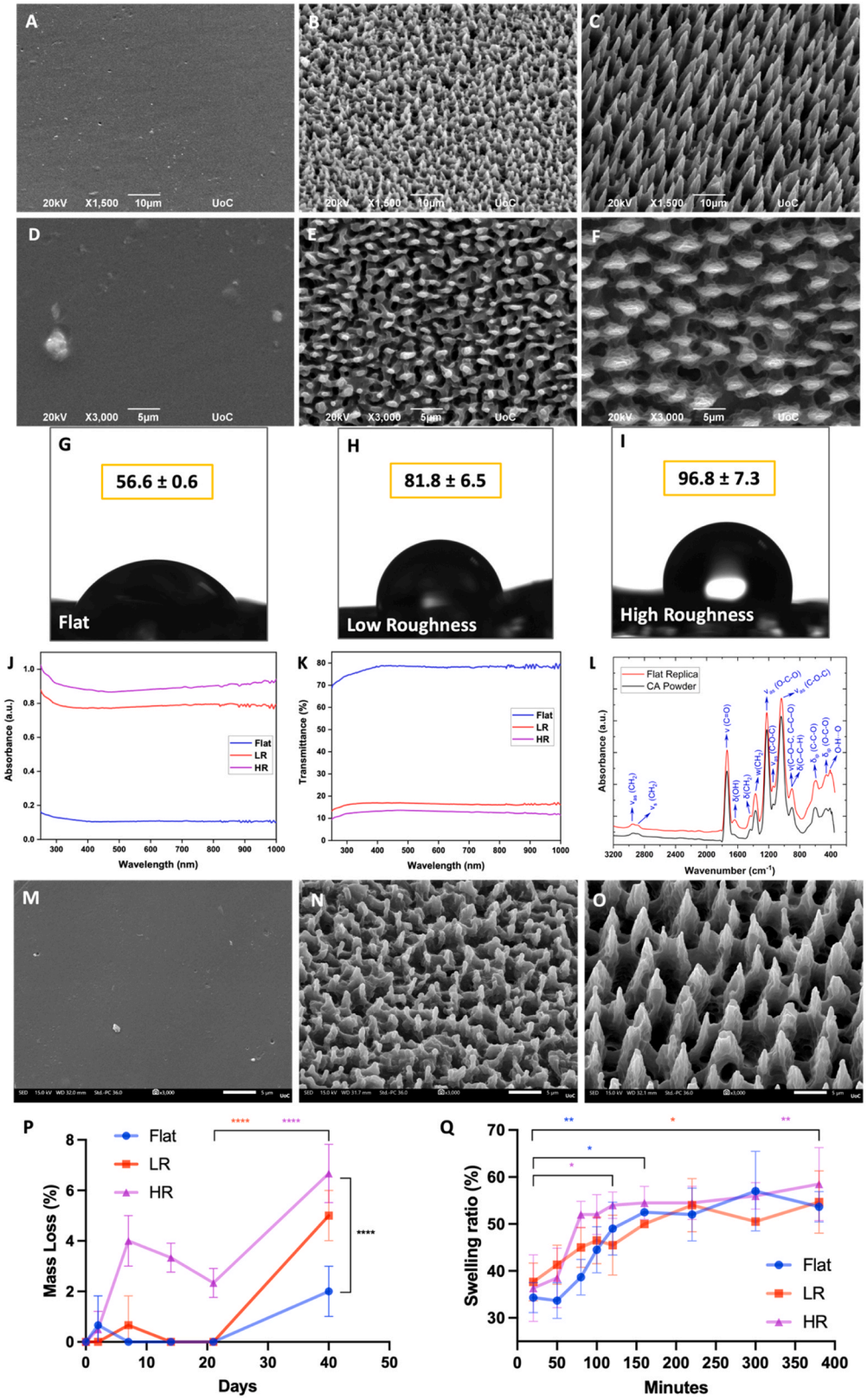

Fig. 1. SEM images **(A–C)**, tilted view, scale bar: 10 μm, and SEM images **(D–F)**, top view, scale bar: 5 μm, of CA replicas with: **A, D)** Flat, **B, E)** Low Roughness and **C, F)** High Roughness topography. Images of water droplets (4 μL) on: **G–I)** CA replicas. **J)** UV-Visible light absorbance, **K)** transmittance spectra and **L)** ATR FT-IR measurements of CA replicas. SEM images (tilted view, scale bar: 5 μm) of the **M)** Flat, **N)** Low & **O)** High Roughness CA replicas, after 40 days of immersion in PBS, at 37 °C. **P)** Mass loss (%) & **Q)** Swelling ratio (%) of the CA replicas. The data were subjected to ANOVA with post hoc Tukey HSD test for multiple comparisons between the groups ($*p \leq 0.05$, $**p \leq 0.01$, $****p \leq 0.0001$), $n = 3$. The error bars denote the standard deviation of the mean.

Wettability and Spectroscopic analysis. CA is generally less hydrophilic than cellulose, due to the substitution of a hydroxyl (-OH) group with acetyl groups. Nevertheless, CA films were generally hydrophilic as reported in literature, for solution-cast [57] or spin-coated thin CA films [58,59]. To assess how both the biomaterial and surface roughness influence wettability, the water contact angle of CA replicas was measured (Fig. 1**(G–I)**).

The flat CA replicas exhibited contact angles in the range of 56.6° ± 0.6°, indicating a hydrophilic surface. The contact angle of LR topographies had values (81.8° ± 6.5°) below 90° and therefore they were considered as hydrophilic. Finally, the measurements obtained for the HR topographies (96.8° ± 7.3°), suggested hydrophobic surfaces. These results indicated a decrease in the hydrophilicity from flat to HR replicas, which was attributed to increased surface roughness.

Surface wettability is an important factor that can affect cell adhesion [60,61], as it reflects the surface free energy, which is defined by interactions at the solid-liquid interface, such as van der Waals forces, electrostatic interactions, and hydrogen bonding. This means that the lower the surface's free energy, the more hydrophobic it is, and thus fewer intermolecular forces are created in the solid - liquid interface [62,63].

While hydrophilic surfaces generally improve cell adhesion, recent studies suggested that rough, hydrophobic surfaces can also promote cell attachment [60]. Padial-Molina et al. demonstrated that osteoblast adhesion increased on rough, hydrophobic surfaces [64], and Kocijan et al., found enhanced osteoblast growth on rough, low-hydrophilicity coatings [65]. Surface wettability is dynamically mediated by proteins during cell adhesion. Proteins may denature by conformational changes during protein adsorption to adjust the surface to the cell's requirements and to compatibilize. While the wettability sensed by the cells may dynamically change, the wettability of the surface may remain constant [66–68].

Furthermore, UV-Vis spectroscopy was performed on various samples across a wavelength range of 250–1000 nm (Fig. 1**(J, K)**), showing behavior consistent with cellulose-based films [69]. The spectra revealed distinct optical properties among the three samples. The Flat sample exhibited minimal light absorption with an absorbance below 0.2, corresponding to a high transmittance of 70–80 %. Conversely, the LR and HR replicas displayed significantly higher absorbance of approximately 0.8 and 0.9, respectively, resulting in markedly reduced transmittance of approximately 15 % and 10 %. These findings indicated that the Flat sample was highly transparent, while the LR and HR replicas exhibited increased opacity due to their denser spike structure.

Fig. 1(L) depicts typical ATR FT-IR measurements, in absorption mode, in a spectral range of 3200 – 350 cm^{-1} for CA powder (green curve) and a typical flat CA replica. Both CA samples exhibit well distinguished weak absorption peaks centered at around 2949 cm^{-1} attributed to the asymmetric stretching mode of CH_2 [ν_{as} CH_2)], 2895 cm^{-1} attributed to the symmetric CH_2 stretching [ν_s (CH_2)] and a strong one centered at around 1735 cm^{-1} which is attributed to the carbonyl stretching mode [ν (C═O)] and a weak one at 1635 cm^{-1} due to deformational vibrations of OH-groups of bound water [δ(OH)] [70,71].

The band at 1436 cm^{-1} is assigned to the bending mode of CH_2 [δ(CH_2)], while the band at 1371 cm^{-1} corresponds to the CH deformation vibration of CH_2 [w(CH_2)] [72–74]. The strong band at 1226 cm^{-1} corresponds to the asymmetric stretching of O-C-O [ν_{as} (O-C-O)] [71–73], while the weak peak at 1145 cm^{-1} band and the strong band at 1039 cm^{-1} corresponds to the asymmetric C-O-C stretching mode from the pyranose ring [ν_{as} (C-O-C)] [71–73,75], while the weak one at ~900 cm^{-1} corresponds to the C-O-C, C-C-O, and C-C-H deformation modes and stretching vibrations of the C-5 and C-6 atoms [ν(C–O–C, C–C–O) & δ(C–C–H) (C-5/C-6)] [71,74]. Finally, the bands at 600 cm^{-1} and 460 cm^{-1} correspond to C-C-O [δ_{ip} (C-C-O)] and O-C-O [δ_{ip} (O-C-O)] in plane deformation vibrations [76], respectively, while the one at ~412 cm^{-1} could be attributed to interactions between hydroxyl groups (-OH) on adjacent glucose units in the cellulose chain, contributing to hydrogen bonding and overall stability of the polymer (O–H···O) [77].

AFM based topography and mechanical analysis. The AFM analysis provided critical information about the mechanical properties of the Flat, LR, and HR replicas. The AFM scans, depicted in a 3D view from the height sensor (Fig. 2**(A–C)**), along with corresponding 2D images of the height sensor and reduced modulus, revealed distinct differences in morphology and stiffness. The corrected (Hertzian fit model) force curves presented in Fig. 2**(D)** and Supplementary Fig. 4, showed that flat replicas had a higher reduced modulus (4300 MPa) compared to LR (950 MPa), and HR replicas (530 MPa) (Fig. 2**(E), (F)**). The differences in mechanical properties at the top of the spikes could be attributed to the soft lithography fabrication technique and the polymer's response to topographical features. The reduced modulus at the peaks of both low and high roughness replicas likely resulted from localized variations in polymer density and stress distribution during fabrication and indentation. The primary difference between LR and HR replica spikes was due to the varying depths of the PDMS mold. In LR replicas, the material filled the mold's shallow spikes (3.59 ± 0.35 μm), whereas HR replicas required more material to fill the deeper spikes (13.06 ± 1.32 μm), resulting in less uniform spikes, especially at the top. This AFM analysis showed how micro-patterned topographical features affect the mechanical behavior of CA replicas, emphasizing their potential to guide cellular responses.

Degradation & Swelling properties of the replicas. Scaffolds degrade *in vivo* through mass loss and shape changes, promoting cell infiltration and controlled drug release [78,79]. Scaffold degradation is influenced by biochemical, physical, geometrical, and mechanical factors, and thus, timely degradation of implanted biomaterials is crucial for successful tissue regeneration. Typically, the degradation occurs in two ways: bulk degradation and surface erosion. The degradation process is usually a combination of these two methods [80,81].

As shown in Fig. 1**(P)**, all replicas exhibited minimal weight loss over time. The Flat replicas had the slowest weight loss than the replicas with microtopographies. Although hydrophobic, the HR topographies had a relatively higher percentage of mass loss. This slight difference could be attributed to the greater surface area of the spikes of the HR replicas, in contact with PBS. Furthermore, the SEM images (Fig. 1**(M–O)**) of the samples after 40 days of immersion suggested the existence of small holes on the spikes of HR samples, while the Flat and LR replicas remained intact.

Various factors, including the material's physicochemical properties and the presence of hydrophilic groups, influence the swelling rate of scaffolds [82]. In the case of CA replicas, the swelling results are presented in Fig. 1**(Q)**. Although all replicas had similar swelling ratios (50–60 %) after 6 h in PBS, LR and HR replicas swelled at a faster rate than the Flat ones. These findings highlighted the impact of scaffold topography on degradation and water absorption.

3.2. *MSCs adhesion, spreading and proliferation on CA biointerfaces*

CA is widely used in drug delivery systems and other biomedical applications due to its biodegradability, non-toxicity, chemical and mechanical persistence, biocompatibility, thermal stability, and suitable cost [39,83]. Although considered biocompatible, the cytotoxicity was assessed. Live/Dead viability assay (Supplementary Fig. 5) showed similar cell proliferation across samples, including controls, with only a few dead cells (red). The samples also had the expected number of dead cells (red). However, in flat topographies, only a few live cells (green) were apparent (Supplementary Fig. 5(B)).

The morphology and adhesion behavior of MSCs cultured on CA biointerfaces and TCP discs were initially evaluated by SEM after 1 and 3 days of culture (Fig. 3**(A–H)**). At day 1, distinct differences in cell morphology were observed across the surfaces. Cells cultured on TCP control samples appeared well-spread and flattened, as expected. In

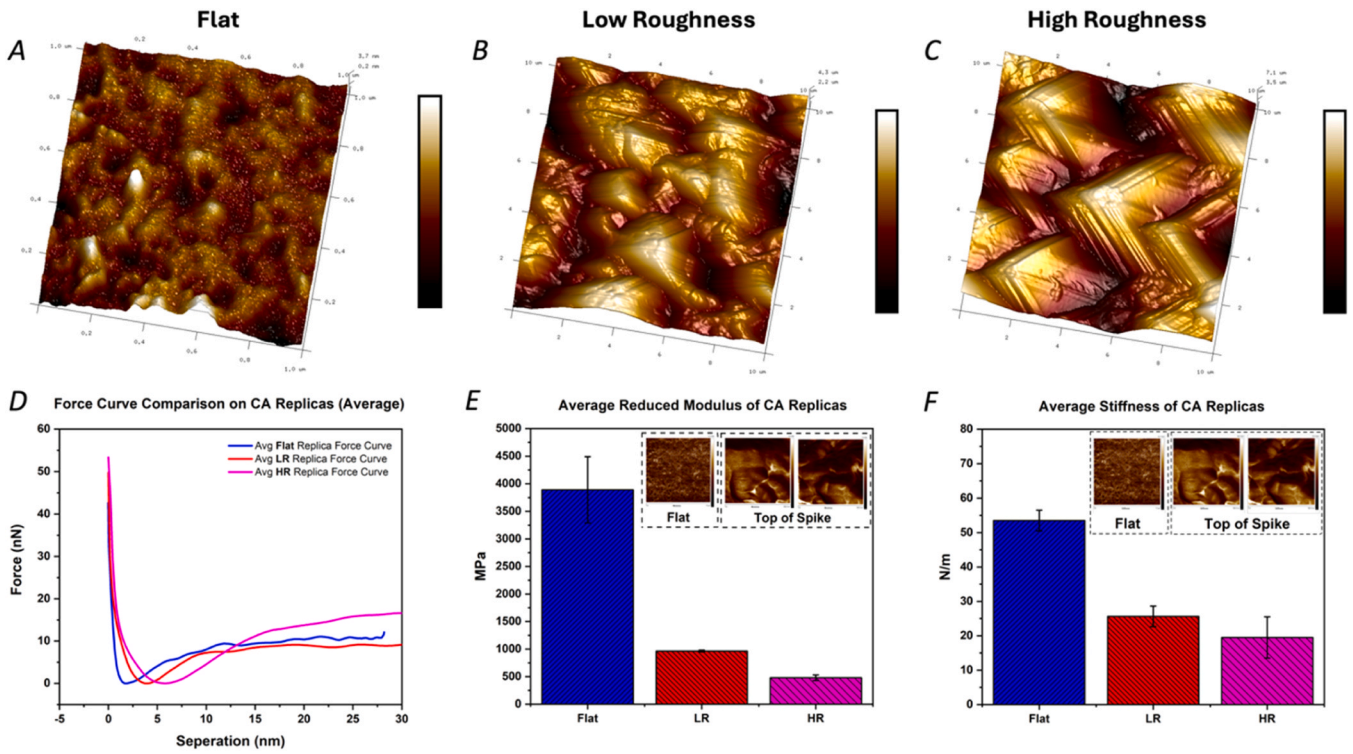

Fig. 2. Schematic figure of the analysis of AFM measurements. **A)** 3D tilted view of the height sensor measurements of the flat CA replica. **B)** 3D tilted view of the height sensor measurements of the LR CA replica. **C)** 3D tilted view of the height sensor measurements of the HR CA replica. **D)** Force curves comparison of CA replicas indicating different force and separation between Flat, LR, and HR replicas. **E)** Average reduced modulus of the CA replicas, indicating that the reduced modulus is significantly reduced as soon as the topography changes from flat to rough (e.g., spikes). Comparison between LR and HR replicas indicated that the higher the roughness, the lower the reduced modulus. **F)** Average stiffness of the CA flat, LR, and HR replicas. For Flat replicas, measurements were focused on the center of the sample, while for LR and HR replicas, measurements were focused on the top of the spike.

contrast, only a few cells adhered to flat surfaces (Fig. 3**(B)**), consistent with the low viability seen in the Live/Dead assay (Supplementary Fig. 5). On Flat and LR topographies (Fig. 3**(B, C)**), cells displayed diverse morphologies, including long spindle-shaped, tripolar-shaped and "star"-like forms. Some dendrite-like and rounded cells could also be detected on the LR samples. On HR topographies (Fig. 3**(D)**), most cells were long, spindle-shaped and aligned along the spikes.

After 3 days (Fig. 3**(E–H)**), the number of attached cells increased across all surfaces, though flat surfaces still showed reduced attachment. Nevertheless, cells on flat topographies demonstrated improved adhesion, appearing more flattened with distinct lamellipodia and projections of filopodia, adopting oblong shapes, *i.e.,* cells with narrow bodies and wide lamellipodia on the edges, whereas tripolar, rounded and "star"-like cells could also be seen. On the control, cells formed a "film"-like surface, as expected. Although cells on the LR samples were elongated after 1 day of culture, on day 3, they appeared more rounded, while oblong, "star"-like, dendrite-like and tripolar cells were still present. In addition, the rounded cells seemed to pull the spikes of the topography with their distinct filopodia. Cells on HR topographies retained their spindle shape and orientation throughout the 3 days of culture.

These observations indicate that MSCs are responsive to surface topography, adjusting their shape and orientation in response to the physical cues provided by the scaffolds. Simitzi et al. [46] proved that micropatterned silicon substrates promote the outgrowth and orientation of neurons and Schwann cells, while Lee et al. [84] demonstrated that micropatterned hydrogels increase MSCs' elongation and cytoskeletal tension, enhancing Runx2 expression. Abagnale et al. [85] concluded that micro-ridges induced alignment and elongation of MSCs' cytoskeleton, promoting osteogenesis. Furthermore, Pan et al. [9] proved that elongated MSCs on hierarchical structures differentiated into osteocytes. McBeath et al. [86] proved that the shape of human MSCs regulated their commitment to osteoblasts or adipocytes. Hence, spreading hMSCs have been shown to become osteocytes, whereas round cells evolved into adipocytes. Although HR biointerfaces exhibited elongated cell morphologies, and according to the literature, they are prone to differentiate into osteocytes, cell fate cannot be predicted based on cell shape alone. To further assess cell adhesion, immunofluorescence staining for paxillin, a focal adhesion (FA) protein [87], was performed (Fig. 3**(I–N),** Supplementary Fig. 6).

Confocal microscopy confirmed the morphological trends observed in SEM, showing fewer adherent cells on Flat samples and more extensive cell spreading on patterned topographies. On Flat and LR biointerfaces, cells exhibited diverse morphologies, like long spindle-shaped, tripolar-shaped and "star"-like. In contrast, HR topographies had perfectly aligned long spindle-shaped, further confirmed by directionality histograms (Fig. 4**(C)**). Additionally, since changes in cell morphology influence the nuclear shape [88,89] the higher nuclear aspect ratio of MSCs on HR biointerfaces (Fig. 3**(O)**), corresponded to uniformly aligned and long spindle-shaped cells through the high roughness spikes.

After 1 day (Fig. 3**(I–N)**), Paxillin was mostly observed as dot-like spots, while by day 3, more mature, dash-like FAs formed at stress fiber ends (Supplementary Fig. 6) [90]. Paxillin expression was more intense on HR topographies, as shown by quantification of mean fluorescence intensity (Fig. 3**(P)**), with HR samples showing higher Paxillin levels than controls after both 1 and 3 days.

After 3 days of culture, confocal images (Supplementary Fig. 6) confirmed that in Flat topographies, the cells did not adhere as well, as in the replicas, while they formed aggregates. MSCs sense the ECM rigidity through FAs. Therefore, the ECM surfaces modulate the spatial distribution, localization, size and maturation states of FAs, which

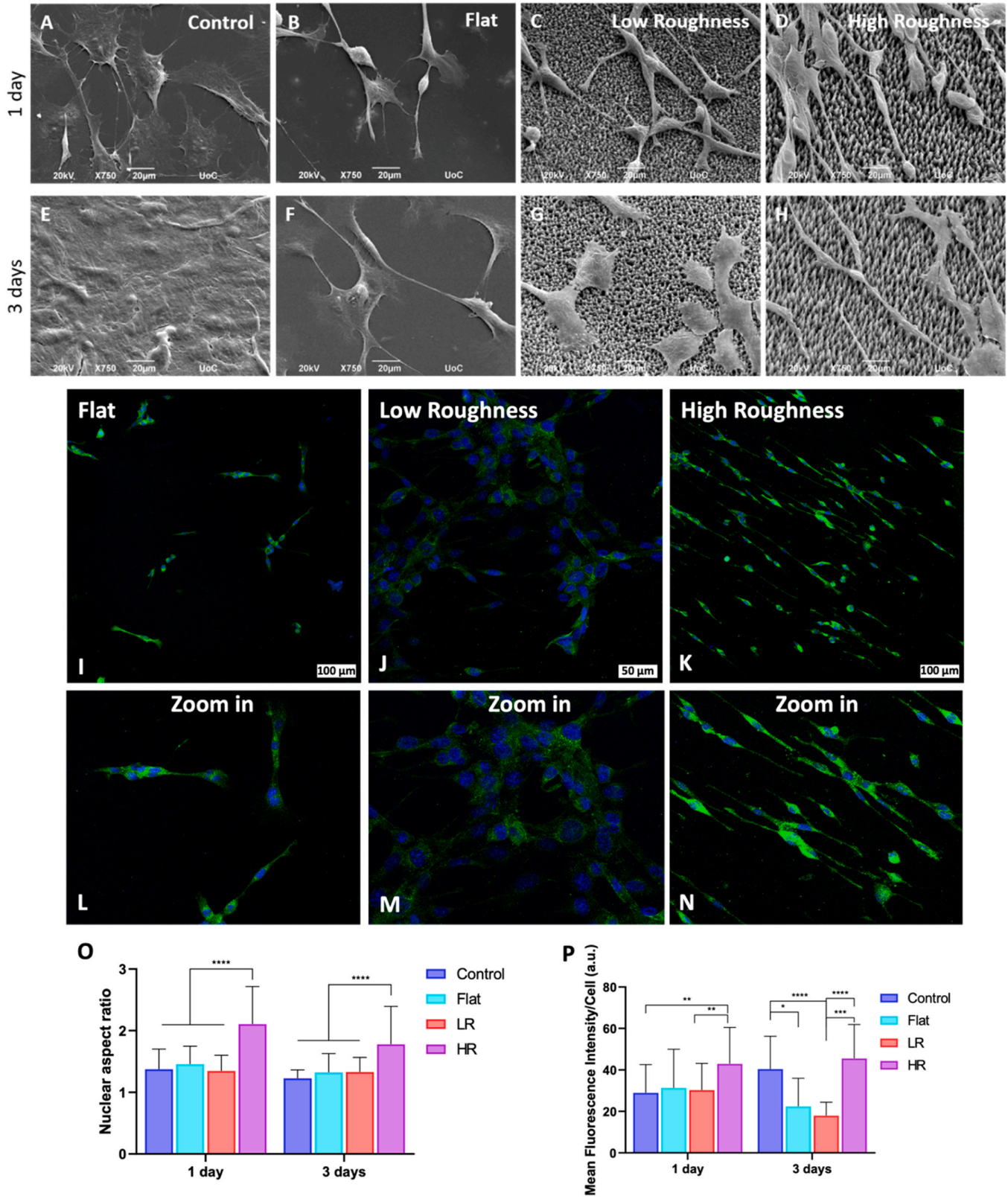

Fig. 3. SEM images (tilted view, scale bar: 20 µm) of MSCs cultured for 1 (**A–D**) and 3 (**E–H**) days on TCP control (**A**, **E**) and CA biointerfaces (**B–D**, **F–H**) with Flat, Low and High Roughness topography. Confocal microscope images (20× or 40× magnification, scale bar: 50 or 100 µm) of MSCs cultured for 1 day on CA biointerfaces (**I–N**), with Flat, Low and High Roughness topography. (Blue: staining of cell nucleus with DAPI, Green: Paxillin staining for focal adhesions). **O)** Nuclear aspect ratio of the MSCs after 1 and 3 days, and **P**) the Mean Fluorescence intensity of Paxillin after 1 and 3 days of culture. The data were subjected to ANOVA with post hoc Tukey HSD test for multiple comparisons between the groups (*$p \leq 0.05$, **$p \leq 0.01$, ***$p \leq 0.001$, ****$p \leq 0.0001$). The error bars denote the standard deviation of the mean.

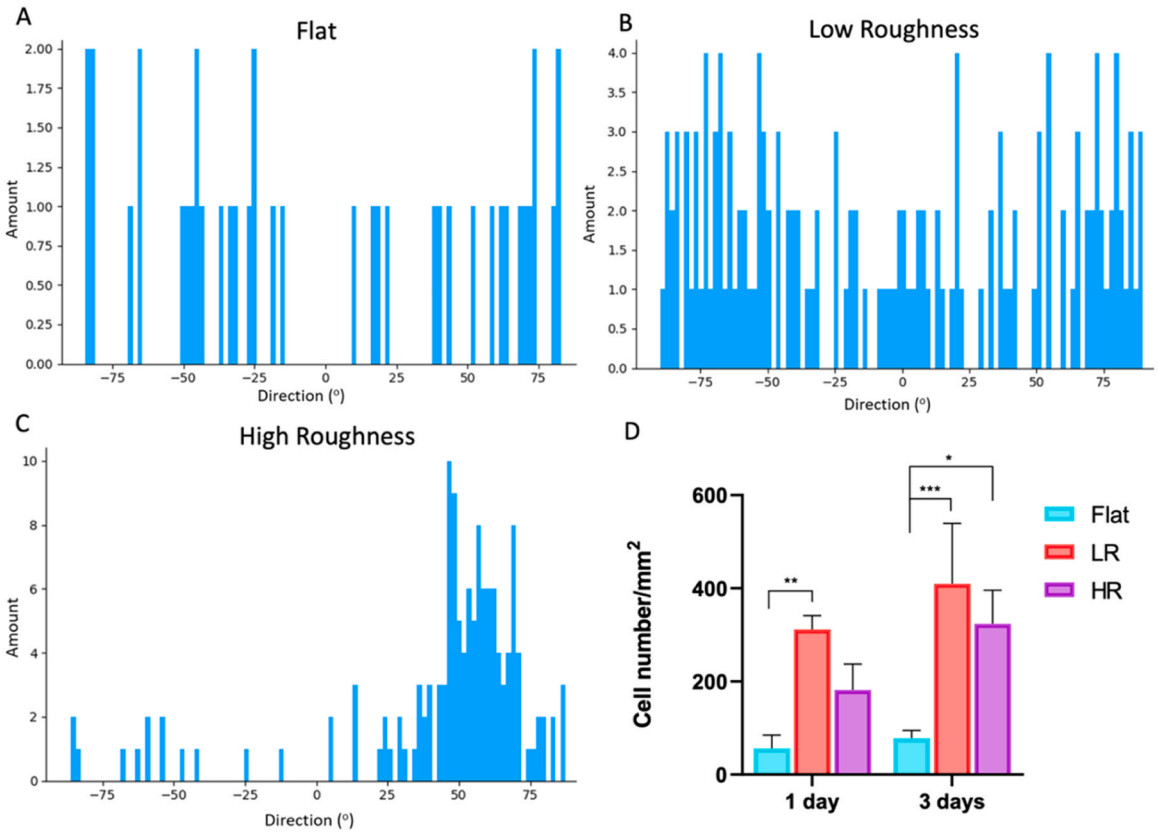

Fig. 4. Directionality histograms **(A–C)** of the cells' direction on the Flat, Low and High Roughness biointerfaces. The histograms were generated using the CellProfiler software, where the "Direction (°)" reports the center of the Gaussian. **D)** MSCs proliferation on CA biointerfaces of all topographies after 1 and 3 days of cell seeding. The data were subjected to ANOVA with post hoc Tukey HSD test for multiple comparisons between the groups (*$p \leq 0.05$, **$p \leq 0.01$, ***$p \leq 0.001$, ****$p \leq 0.0001$). The error bars denote the standard deviation of the mean.

transduce integrin-mediated signals to remodel the cytoskeleton and program gene expression for specific biological outcomes, including cell shape, survival, growth, migration and differentiation [32]. After 1 day, all samples expressed immature FAs. This changed on day 3, where mature FAs were obvious. More specifically, the LR topography experienced very good cell attachment.

Finally, MSCs proliferation was quantified after 1 and 3 days of culture (Fig. 4**(D)**). Flat biointerfaces supported the lowest cell proliferation, after both 1 and 3 days, while LR bionterfaces showed the highest proliferation. HR samples exhibited an intermediate level of proliferation capacity. An increase in cell proliferation was seen across all samples after 3 days of culture. Together, these data suggest that while LR topographies promote robust cell attachment and proliferation, HR topographies support strong adhesion and alignment, potentially leading cells toward osteocyte-like differentiation.

3.3. Mechanoresponse of MSCs on microtopographies

The cellular localization of YAP/TAZ can be used as an indicator of cellular response to a specific substrate. YAP/TAZ are imported into the cell nuclei when cultured on a large surface area, a stiff matrix or in the presence of mechanical forces [17,91,92]. However, YAP/TAZ are translocated into the cytoplasm when cells are cultured on soft matrices or at high cellular densities [93,94]. To investigate the mechanosensitive response of MSCs to replicas topography, the subcellular localization of TAZ in MSCs, under standard and osteogenic conditions, was examined. Representative immunofluorescence images are shown in Supplementary Figs. 7, 8, and quantitative analysis is presented in Fig. 5 **(A, B)**.

In summary, flattened cells on control, Flat and LR topographies expressed nuclear TAZ, while TAZ in long spindle-shaped cells of HR samples, shuttled in the cytoplasm. The nuclear to cytoplasmic TAZ ratio (Fig. 5**(A, B)**) showed consistent values in control samples, with a slight increase under osteogenic conditions, likely due to osteogenesis. The increased nuclear-to-cytoplasmic ratio after 8 days in standard media was attributed to material stiffness as proved by AFM measurements, especially on flat samples. These values were significantly decreased over time, possibly due to higher cell density, which was proposed from the literature to translocate TAZ into the cytoplasm. With OSTEO medium, nuclear TAZ localization increased across all samples. In osteogenic conditions, the nuclear-to-cytoplasmic ratio of the Flat was increased after 15 days. On LR biointerfaces, a constant augmentation of nuclear TAZ was observed throughout the timepoints. To conclude, it seemed that the LR topographies, as well as the material itself (Flat sample) favor the nuclear localization of TAZ, which could be an indicator of enhanced osteogenesis, while HR samples had reduced nuclear TAZ, reflecting their long spindle-shaped cell morphology.

Hou et al. [95] demonstrated that nuclear YAP accumulation increases with substrate roughness up to an intermediate level, then decreases at higher roughness, with intermediate roughness showing the highest osteogenesis. Yang et al. [96] found that hydroxyapatite substrates with ~1.09μm roughness promoted strong osteogenic differentiation of MSCs and elevated YAP/TAZ expression. The current research aligns with the literature, indicating that the intermediate roughness of LR biointerfaces induces the nuclear translocation of TAZ and potentially osteogenesis, though further validation is needed.

3.4. Osteogenic differentiation of MSCs on microtopographies

To evaluate the osteogenic potential of the CA biointerfaces, MSCs

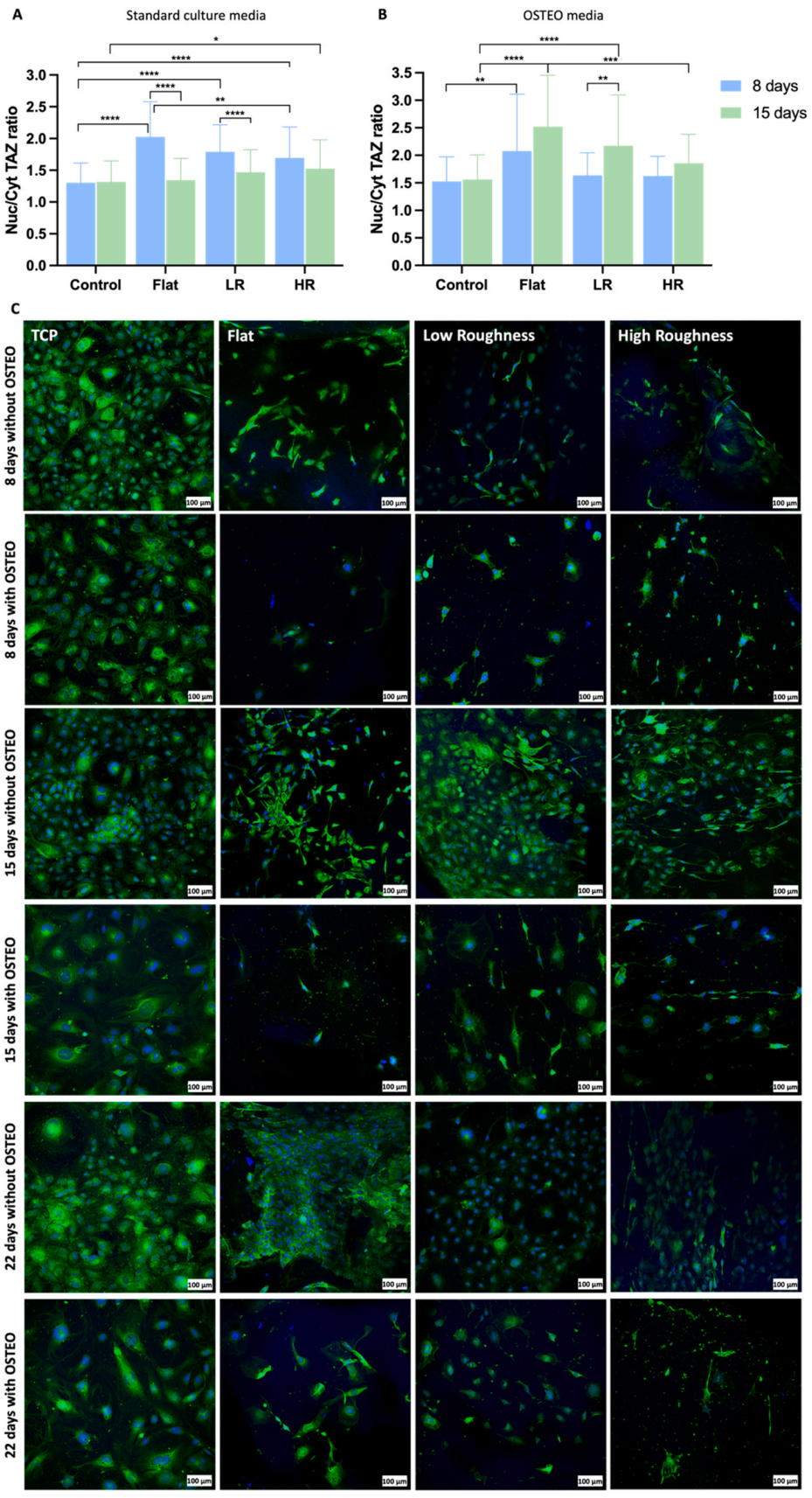

(caption on next page)

Fig. 5. Quantification of the Nuclear/Cytoplasmic TAZ, when MSCs are cultured on control and CA biointerfaces of Flat, Low and High Roughness topography, for 8 and 15 days with **A)** standard culture medium and **B)** osteogenic medium. The data were subjected to ANOVA with post hoc Tukey HSD test for multiple comparisons between the groups (*p ≤ 0.05, **p ≤ 0.01, ***p ≤ 0.001, ****p ≤ 0.0001). The error bars denote the standard deviation of the mean. **C)** Confocal microscope images (20x magnification, scale bar: 100 μm) of MSCs on TCP coverslips, Flat, Low and High Roughness CA biointerfaces, cultured for 8, 15 and 22 days in both standard and osteogenic culture medium. (Blue: staining of cell nucleus with DAPI, Green: Osteopontin expression staining).

were cultured on Flat, LR, and HR biointerfaces under both standard and osteogenic (OSTEO) conditions. The expression of key osteogenic markers—osteopontin (OPN), associated with mid-to-late stages [97], and alkaline phosphatase (ALP), an early-stage marker [98,99]—was assessed *via* immunofluorescence at 8, 15, and/or 22 days (Figs. 5**(C),** 6). OPN is crucial for bone remodeling and responds to mechanical stress [100,101], while ALP supports matrix mineralization by regulating inorganic phosphates and pyrophosphate [98,102].

Osteopontin Expression. After 8 days, all surfaces supported OPN expression, with relatively uniform staining across conditions (Fig. 5**(C),** Supplementary Figs. 9(A), 10). At day 15, MSCs cultured in standard medium showed increased OPN levels on all CA biointerfaces, particularly on LR topographies (Fig. 5**(C),** Supplementary Fig. 11), while expression in OSTEO controls decreased slightly (Fig. 5**(C),** Supplementary Fig. 12). Notably, OPN expression remained elevated on LR samples even in the absence of osteogenic supplements, suggesting that intermediate topography alone can stimulate osteogenic signaling (Supplementary Fig. 9(B)). By day 22, OPN expression remained increased on the standard control (Fig. 5**(C),** Supplementary Figs. 9(B), 13), whereas expression in OSTEO-treated groups plateaued or declined (Fig. 5**(C),** Supplementary Fig. 14). OPN levels remained increased in the standard Flat sample, while in the standard LR biointerfaces, OPN expression was slightly decreased, suggesting a temporal regulation of topography-induced signaling (Supplementary Fig. 9(B)). Morphologically, cells on LR biointerfaces transitioned to rounded and enlarged forms resembling osteoblast-like phenotypes, consistent with enhanced

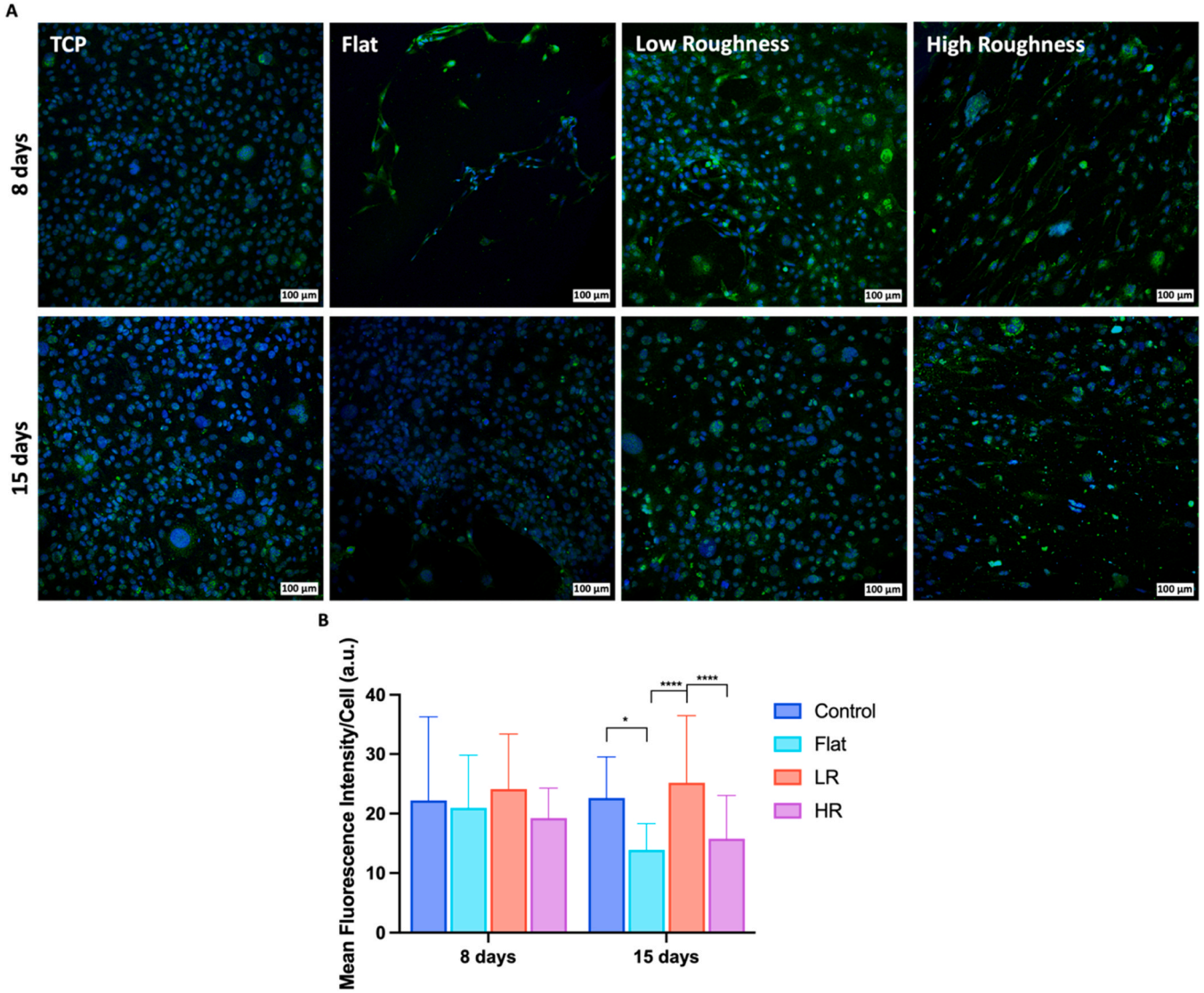

Fig. 6. A) Confocal microscope images (20× magnification, scale bar: 100 μm) of MSCs on TCP control coverslips and CA biointerfaces of Flat, Low and High Roughness, cultured for 8 and 15 days in both standard and osteogenic culture medium. (Blue: staining of cell nucleus with DAPI, Green: Alkaline phosphatase expression staining). **B)** Mean Fluorescence intensity of ALP after 8 and 15 days of culture. The data were subjected to ANOVA with post hoc Tukey HSD test for multiple comparisons between the groups (*p ≤ 0.05, ****p ≤ 0.0001). The error bars denote the standard deviation of the mean.

OPN expression. In contrast, HR biointerfaces continued to support elongated, aligned cells with dendrite-like projections, reminiscent of osteocyte morphology, though with stable or slightly lower OPN levels. Overall, OPN expression followed a topography- and time-dependent pattern, with LR biointerfaces possibly supporting earlier and more pronounced osteogenic commitment compared to Flat and HR topographies. For clarity, the main trends of OPN expression across topographies and timepoints are summarized in Table 2.

Alkaline Phosphatase Expression. ALP expression was evaluated after 8 and 15 days. After 8 days (Fig. 6 **and** Supplementary Fig. 15), the highest ALP expression was noted in MSCs on LR biointerfaces, where staining localized to both the nucleus and cytoplasm. HR biointerfaces also supported strong ALP expression, primarily in the cytoplasm of elongated cells. Less ALP-positive cells were found on flat surfaces.

At 15 days (Fig. 6 **and** Supplementary Fig. 16), ALP levels decreased in all samples, in agreement with known ALP temporal dynamics—peaking early and tapering as cells progress toward matrix mineralization. As aforementioned, ALP is an early osteogenic marker, with the highest peak after 15 days of culture, as also reported by Park et al. [103] and Hanna et al. [104]. In our case, the expression of ALP, on flat and HR bionterfaces, seemed to be higher at 8 days and slightly decreased after 15 days. Therefore, we suggest the synergistic effect of stiffness and topography in inducing early MSCs osteogenesis, with LR topography presenting the most interesting results. The LR presented higher ALP expression compared to all tested biointerfaces, both at 8 and 15 days (Fig. 6**(B)**). Interestingly, a correlation between cell morphology and ALP localization emerged. Rounded and enlarged cells on LR biointerfaces exhibited both nuclear and cytoplasmic ALP staining, whereas elongated cells on HR biointerfaces primarily showed cytoplasmic expression.

The overall physicochemical, surface-mechanical and biological results of this study are summarized in Table 2. Taken together, these results indicate that LR micro-topographies provide optimal mechanical–topographical cues for early osteogenic commitment, likely through enhanced cell spreading, increased focal adhesion maturation, and sustained TAZ nuclear localization, indicating active mechanotransductive signaling. Meanwhile, HR surfaces characterized by lower interfacial stiffness and strong contact-guidance alignment, appear to bias MSCs toward osteocyte-like phenotypes. Flat CA biointerfaces supported limited adhesion and osteogenic activity, consistent with their high stiffness but lack of topographical cues.

These findings highlight that osteogenic commitment on CA biointerfaces arises from a synergistic interplay between local stiffness and microstructure, and they suggest that LR biointerfaces create an optimal biomechanical microenvironment capable of promoting bone-related differentiation even in the absence of exogenous osteoinductive

Table 2
Summary of the physicochemical, surface-mechanical and biological characteristics of CA bionterfaces in standard and OSTEO medium. Arrows represent semi-quantitative trends derived from image-based analysis: (* = low; ** = medium, *** = high; 8 D = 8 days, in light grey color; 15 D = 15 days, in medium grey color; 22 D = 22 days, in dark grey color).

Topography	Spikes Height	Wettability	Reduced Modulus
Flat	–	Hydrophilic	4300 MPa
LR	2.43 ± 0.19 μm	Hydrophilic	950 MPa
HR	9.19 ± 0.66 μm	Hydrophobic	530 MPa

Topography	Adhesion	Proliferation	TAZ (Nuc/Cyt)		OPN			ALP	
			8 D	15 D	8 D	15 D	22 D	8 D	15 D
			Standard medium						
Flat	*	*	***	*	**	***	***	***	**
			OSTEO		*OSTEO*				
			**	***	**	**	*		
			Standard medium						
LR	**	***	***	**	**	***	***	***	***
			OSTEO		*OSTEO*				
			*	***	***	***	**		
			Standard medium						
HR	*** (strong alignment)	**	***	**	**	***	***	***	**
			OSTEO		*OSTEO*				
			*	**	***	***	*		

factors. In this context, recent biomaterial-based strategies, including advanced scaffold systems, cell-free extracellular matrix–inspired approaches, and engineered instructive microenvironments, have also demonstrated the potential of robust biomaterial platforms to enhance bone regeneration [105–109].

4. Conclusion

The interplay between scaffold topography and mechanical properties plays a pivotal role in directing stem cell response in bone tissue engineering (BTE). This study demonstrated that mesenchymal stem cells (MSCs) respond sensitively to the interfacial mechanics of cellulose acetate (CA) microstructured biointerfaces, with these physical cues modulating adhesion, cytoskeletal organization and early osteogenic commitment. Atomic force microscopy revealed a clear coupling between surface roughness and local stiffness, as increasing topographical height reduced the reduced modulus at the spike apex.

While high roughness (HR) biointerfaces supported aligned, elongated cell morphologies, their lower stiffness correlated with diminished nuclear localization of the mechanosensitive regulator TAZ, indicating attenuated mechanotransductive activity. In contrast, low roughness (LR) biointerfaces provided an optimal combination of microstructure and interfacial stiffness, promoting focal adhesion maturation, enhanced nuclear TAZ localization, and upregulated expression of early-to-middle osteogenic markers such as ALP and OPN.

These findings reinforce that both topography and stiffness are key regulators of MSCs fate, likely acting through mechanosensitive pathways involving TAZ. Notably, LR biointerfaces induced osteogenic commitment even in the absence of biochemical inducers, supporting their potential as cell-instructive biointerfaces. This work establishes a mechanistic link between microstructure-mediated interfacial mechanics and MSCs osteogenic commitment, highlighting CA as a sustainable platform for designing biointerfaces with tailored mechanical–topographical cues. Fluorescence-based evaluation of osteogenic markers was employed to examine spatiotemporal correlation between osteogenic signaling, cell morphology, and TAZ-mediated mechanotransduction across topographies, timepoints and culture conditions. However, extended biochemical (e.g., p-NPP, Alizarin Red assay) and molecular analyses (e.g., RT-PCR) are required to fully validate the osteogenic phenotype. Future work exploring downstream osteogenic regulators (e.g., RUNX2, Osterix, Sclerostin) will further clarify how these physical signals guide cell fate and will support the rational development of next-generation scaffolds for clinical BTE applications.

From a translational point of view, the potential of CA microstructured replicas to promote osteogenic commitment through physical cues is particularly relevant for BTE applications. Such biointerfaces could reduce the use of exogenous osteoinductive factors, simplifying scaffold design. Importantly, CA is compatible with scalable manufacturing approaches, including 3D printing techniques, which could be combined to generate hierarchical 3D scaffolds with micro-topographical features. Given the biocompatibility, processability, and scalability of CA, these biointerfaces represent promising candidates for future implantable platforms in bone repair.

CRediT authorship contribution statement

Paraskevi Kavatzikidou: Writing – review & editing, Methodology, Investigation, Formal analysis, Conceptualization. **Eleni Kanakousaki:** Writing – original draft, Methodology, Investigation, Formal analysis, Conceptualization. **Konstantina Alexaki:** Writing – review & editing, Investigation, Formal analysis. **Panagiotis Daskalakis:** Writing – review & editing, Methodology, Investigation, Formal analysis, Conceptualization. **Alexandra Manousaki:** Investigation. **Stella Maragkaki:** Writing – review & editing, Investigation, Formal analysis. **Jagrati Dwivedi:** Investigation. **Keller Thomas:** Writing – review & editing, Formal analysis. **George Kenanakis:** Writing – review & editing, Investigation, Formal analysis. **Anthi Ranella:** Writing – review & editing, Validation, Supervision, Funding acquisition, Conceptualization. **Emmanuel Stratakis:** Writing – review & editing, Supervision, Funding acquisition, Conceptualization.

Declaration of Generative AI and AI-assisted technologies in the writing process

Generative AI tools were used solely for language refinement. The authors take full responsibility for the content of the published article.

Data availability

This is an open access publication. The manuscript and supplementary data and information can be accessible to the readers upon request. The data are stored in an Institutional cloud link with access to all the authors during the writing and submission process of the manuscript. The cloud link will stay as is in the Institution.

Declaration of Competing Interest

The authors declare that they have no known competing financial interests or personal relationships that could have appeared to influence the work reported in this paper.

Acknowledgements

The authors would like to thank Alexander Meinhardt for his assistance in operating the AFM instrument at the DESY NanoLab. This work was supported by NFFA EUROPE Pilot (EU H2020 framework programme) under Grant agreement no. 101007417 and the “Theodore Papazoglou” FORTH Synergy Grants (StatinCensor) for providing financial support to this project.

Appendix A. Supporting information

Supplementary data associated with this article can be found in the online version at doi:10.1016/j.mtcomm.2026.114808.

Data availability

Data will be made available on request.

References

[1] M.R. Iaquinta, et al., Adult stem cells for bone regeneration and repair, Front. Cell Dev. Biol. 7 (2019) 268.
[2] R. Núñez-Toldrà, et al., Dental pulp pluripotent-like stem cells (DPPSC), a new stem cell population with chromosomal stability and osteogenic capacity for biomaterials evaluation, BMC Cell Biol. 18 (2017).
[3] N. Abbasi, S. Hamlet, R.M. Love, N.T. Nguyen, Porous scaffolds for bone regeneration, J. Sci. Adv. Mater. Devices 5 (2020) 1–9.
[4] B. Stevens, Y. Yang, A. Mohandas, B. Stucker, K.T. Nguyen, A review of materials, fabrication methods, and strategies used to enhance bone regeneration in engineered bone tissues, J. Biomed. Mater. Res. Part B Appl. Biomater. 85B (2008) 573–582.
[5] A.W. Orr, B.P. Helmke, B.R. Blackman, M.A. Schwartz, Mechanisms of mechanotransduction, Dev. Cell 10 (2006) 11–20.
[6] H. Niu, et al., Surface topography regulates osteogenic differentiation of MSCs via crosstalk between FAK/MAPK and ILK/β-catenin pathways in a hierarchically porous environment, ACS Biomater. Sci. Eng. 3 (2017) 3161–3175.
[7] The draft Materials 2030 roadmap | Materials 2030 Initiative. ⟨https://www.ami2030.eu/roadmap/⟩.
[8] C.Y. Yang, et al., Neural tissue engineering: the influence of scaffold surface topography and extracellular matrix microenvironment, J. Mater. Chem. B 9 (2021) 567–584.
[9] H. Pan, et al., YAP-mediated mechanotransduction regulates osteogenic and adipogenic differentiation of BMSCs on hierarchical structure, Colloids Surf. B Biointerfaces 152 (2017) 344–353.

[10] S. Chen, et al., Tuning surface properties of bone biomaterials to manipulate osteoblastic cell adhesion and the signaling pathways for the enhancement of early osseointegration, Colloids Surf. B Biointerfaces 164 (2018) 58–69.
[11] Y. Hou, et al., Surface roughness and substrate stiffness synergize to drive cellular mechanoresponse, Nano Lett. 20 (2020) 748–757.
[12] P. Haftbaradaran Esfahani, R. Knöll, Cell shape: effects on gene expression and signaling, Biophys. Rev. 12 (2020) 895–901.
[13] T. Gong, et al., Dynamically tunable polymer microwells for directing mesenchymal stem cell differentiation into osteogenesis, J. Mater. Chem. B 3 (2015) 9011–9022.
[14] H. Lai, B. Gong, J. Yin, J. Qian, 3D printing topographic cues for cell contact guidance: a review, Mater. Des. 218 (2022) 110663.
[15] Z. Sun, S.S. Guo, R. Fässler, Integrin-mediated mechanotransduction, J. Cell Biol. 215 (2016) 445–456.
[16] M.K. Kim, J.W. Jang, S.C. Bae, DNA binding partners of YAP/TAZ, BMB Rep. 51 (2018) 126–133.
[17] M. Zarka, E. Haÿ, M. Cohen-Solal, YAP/TAZ in bone and cartilage biology, Front. Cell Dev. Biol. 9 (2022) 3535.
[18] M.R. Byun, et al., FGF2 stimulates osteogenic differentiation through ERK induced TAZ expression, Bone 58 (2014) 72–80.
[19] C. Lorthongpanich, et al., YAP as a key regulator of adipo-osteogenic differentiation in human MSCs, Stem Cell Res. Ther. 10 (2019) 1–12.
[20] Q. Wei, et al., BMP-2 signaling and mechanotransduction synergize to drive osteogenic differentiation via YAP/TAZ, Adv. Sci. 7 (2020) 1902931.
[21] J.X. Pan, et al., YAP promotes osteogenesis and suppresses adipogenic differentiation by regulating β-catenin signaling, Bone Res. 61 (6) (2018) 1–12.
[22] The role of nonmuscle myosin 2A and 2B in the regulation of mesenchymal cell contact guidance, 2019. ⟨https://doi.org/10.1091/mbc.E19-01-0071⟩.
[23] Q. Wang, Y. Huang, Z. Qian, Nanostructured surface modification to bone implants for bone regeneration, J. Biomed. Nanotechnol. 14 (2018) 628–648.
[24] Y. Du, et al., Topographic cues of a novel bilayered scaffold modulate dental pulp stem cells differentiation by regulating YAP signalling through cytoskeleton adjustments, Cell Prolif. 52 (2019).
[25] L. Yang, K.M. Jurczak, L. Ge, P. van Rijn, High-throughput screening and hierarchical topography-mediated neural differentiation of mesenchymal stem cells, Adv. Healthc. Mater. 9 (2020).
[26] L. Yang, et al., Topography induced stiffness alteration of stem cells influences osteogenic differentiation, Biomater. Sci. 8 (2020) 2638–2652.
[27] X. Cun, L. Hosta-Rigau, Topography: a biophysical approach to direct the fate of mesenchymal stem cells in tissue engineering applications, Nanomater 10 (2020) 2070.
[28] K. Dave, V.G. Gomes, Interactions at scaffold interfaces: effect of surface chemistry, structural attributes and bioaffinity, Mater. Sci. Eng. C 105 (2019) 110078.
[29] Y. Hou, et al., Surface roughness gradients reveal topography-specific mechanosensitive responses in human mesenchymal stem cells, Small 16 (2020).
[30] W.H. Goldmann, Role of vinculin in cellular mechanotransduction, Cell Biol. Int. 40 (2016) 241–256.
[31] L.B. Case, et al., Molecular mechanism of vinculin activation and nanoscale spatial organization in focal adhesions, Nat. Cell Biol. 17 (2015) 880–892.
[32] J.C. Kuo, Focal adhesions function as a mechanosensor, Prog. Mol. Biol. Transl. Sci. 126 (2014) 55–73.
[33] K. Zhou, T. Yuan, S. Wang, F. Hu, L. Luo, L. Chen, L. Yang, Beyond natural silk: bioengineered silk fibroin for bone regeneration, Mater. Today Bio 33 (2025) 102014.
[34] B. Zheng, J. Xing, X. Tang, Z. He, Q. Tang, S. Liu, Y. Xiao, J. Xu, E. Luo, Y. Liu, Tailored surface topographical scaffolds: a breakthrough in osteoarthritic cartilage and subchondral bone defect repair, J. Mater. Chem. B. 13 (2025) 8639–8652.
[35] T. Ogawa, R. Shibata, K. Komatsu, T. Matsuura, D. Chao, W. Park, M. Hirota, Bridging the missing middle in osseointegration: meso-scale topography between macro design and microroughness, Int. J. Implant Dent. 11 (1) (2025) 68.
[36] B.D. Gates, Nanofabrication with molds & stamps, Mater. Today 8 (2005) 44–49.
[37] Xia Y., Whitesides G.M., Soft lithography, vol. 28, 2003, pp. 153–84. ⟨https://doi.org/10.1146/annurev.matsci.28.1.153⟩.
[38] O. Sahin, M. Ashokkumar, P.M. Ajayan, Micro- and nanopatterning of biomaterial surfaces, Fundam. Biomater. Met. (2018) 67–78, https://doi.org/10.1016/B978-0-08-102205-4.00003-9.
[39] K. Khoshnevisan, et al., Cellulose acetate electrospun nanofibers for drug delivery systems: applications and recent advances, Carbohydr. Polym. 198 (2018) 131–141.
[40] S. Fischer, et al., Properties and applications of cellulose acetate, Macromol. Symp. 262 (2008) 89–96.
[41] M.A. Wsoo, S. Shahir, S.P. Mohd Bohari, N.H.M. Nayan, S.I.A. Razak, A review on the properties of electrospun cellulose acetate and its application in drug delivery systems: a new perspective, Carbohydr. Res. 491 (2020) 107978.
[42] S. Zuppolini, A. Salama, I. Cruz-Maya, V. Guarino, A. Borriello, Cellulose amphiphilic materials: chemistry, process and applications, Pharmaceutics 14 (2022) 386.
[43] E. Babaliari, et al., Engineering cell adhesion and orientation via ultrafast laser fabricated microstructured substrates, Int. J. Mol. Sci. 19 (2018).
[44] D. Angelaki, P. Kavatzikidou, C. Fotakis, E. Stratakis, A. Ranella, Laser-structured Si and PLGA inhibit the Neuro2a differentiation in mono- and co-culture with glia, Tissue Eng. Regen. Med. 20 (2023) 111–125.
[45] D. Angelaki, P. Kavatzikidou, C. Fotakis, E. Stratakis, A. Ranella, Laser-induced topographies enable the spatial patterning of co-cultured peripheral nervous system cells, Mater. Sci. Eng. C 115 (2020) 111144.
[46] C. Simitzi, et al., Laser fabricated discontinuous anisotropic microconical substrates as a new model scaffold to control the directionality of neuronal network outgrowth, Biomaterials 67 (2015) 115–128.
[47] C. Simitzi, E. Stratakis, C. Fotakis, I. Athanassakis, A. Ranella, Microconical silicon structures influence NGF-induced PC12 cell morphology, J. Tissue Eng. Regen. Med. 9 (2015) 424–434.
[48] A. Stierle, T.F. Keller, H. Noei, V. Vonk, R. Roehlsberger, DESY NanoLab, J. Large-Scale Res. Facil. JLSRF 2 (2016) A76.
[49] A. Meinhardt, P. Lakner, P. Huber, T.F. Keller, Mapping the nanoscale elastic property modulations of polypyrrole thin films in liquid electrolyte with EC-AFM, Nanoscale Adv. 6 (2023) 102–110.
[50] D. Wang, T.P. Russell, Advances in atomic force microscopy for probing polymer structure and properties, Macromolecules 51 (2018) 3–24.
[51] H.J. Butt, B. Cappella, M. Kappl, Force measurements with the atomic force microscope: technique, interpretation and applications, Surf. Sci. Rep. 59 (2005) 1–152.
[52] J. Schindelin, et al., Fiji: an open-source platform for biological-image analysis, Nat. Methods 97 (9) (2012) 676–682.
[53] D.R. Stirling, et al., CellProfiler 4: improvements in speed, utility and usability, BMC Bioinform. 22 (2021) 1–11.
[54] L. Kamentsky, et al., Improved structure, function and compatibility for CellProfiler: modular high-throughput image analysis software, Bioinformatics 27 (2011) 1179–1180.
[55] A.E. Carpenter, et al., CellProfiler: image analysis software for identifying and quantifying cell phenotypes, Genome Biol. 7 (2006) 1–11.
[56] P. Daskalakis, E. Kanakousaki, C. Ntoulias, K. Peponaki, P. Kavatzikidou, A. Manousaki, D. Vlassopoulos, A. Ranella, E. Stratakis, 3D bioprinting with high-viscosity bioinks: a custom-designed extrusion head for high resolution cellulose acetate scaffolds, Int. J. Bioprint. (2025) 25060047.
[57] S. Wu, X. Qin, M. Li, The structure and properties of cellulose acetate materials: a comparative study on electrospun membranes and casted films, J. Ind. Text. 44 (2014) 85–98.
[58] A. Kramar, I. Rodríguez Ortega, G. González-Gaitano, J. González-Benito, Solution casting of cellulose acetate films: influence of surface substrate and humidity on wettability, morphology and optical properties, Cellulose 30 (2023) 2037–2052.
[59] F. Mikaeili, P.I. Gouma, Super water-repellent cellulose acetate mats, Sci. Rep. 8 (2018).
[60] A. Ranella, M. Barberoglou, S. Bakogianni, C. Fotakis, E. Stratakis, Tuning cell adhesion by controlling the roughness and wettability of 3D micro/nano silicon structures, Acta Biomater. 6 (2010) 2711–2720.
[61] W. Song, D.D. Veiga, C.A. Custódio, J.F. Mano, Superhydrophobic coatings: bioinspired degradable substrates with extreme wettability properties (Adv. Mater. 18/2009), Adv. Mater. 21 (2009).
[62] M.E. Callow, R.L. Fletcher, The influence of low surface energy materials on bioadhesion — a review, Int. Biodeterior. Biodegrad. 34 (1994) 333–348.
[63] K. Anselme, et al., The interaction of cells and bacteria with surfaces structured at the nanometre scale, Acta Biomater. 6 (2010) 3824–3846.
[64] M. Padial-Molina, et al., Role of wettability and nanoroughness on interactions between osteoblast and modified silicon surfaces, Acta Biomater. 7 (2011) 771–778.
[65] A. Kocijan, M. Conradi, M. Hočevar, The influence of surface wettability and topography on the bioactivity of TiO2/epoxy coatings on AISI 316L stainless steel, Materials 12 (2019) 1877.
[66] L. Vroman, A.L. Adams, Identification of rapid changes at plasma–solid interfaces, J. Biomed. Mater. Res. 3 (1969) 43–67.
[67] P. Turbill, T. Beugeling, A.A. Poot, Proteins involved in the Vroman effect during exposure of human blood plasma to glass and polyethylene, Biomaterials 17 (1996) 1279–1287.
[68] T.F. Keller, et al., How the surface nanostructure of polyethylene affects protein assembly and orientation, ACS Nano 5 (2011) 3120–3131.
[69] H. Orelma, et al., Optical cellulose fiber made from regenerated cellulose and cellulose acetate for water sensor applications, Cellulose 27 (2020) 1543–1553.
[70] N. Atykyan, V. Revin, V. Shutova, Raman and FT-IR Spectroscopy investigation the cellulose structural differences from bacteria Gluconacetobacter sucrofermentans during the different regimes of cultivation on a molasses media, AMB Express 10 (2020) 1–11.
[71] S.Y. Oh, D. Yoo, Il, Y. Shin, G. Seo, FTIR analysis of cellulose treated with sodium hydroxide and carbon dioxide, Carbohydr. Res. 340 (2005) 417–428.
[72] L.M. Proniewicz, et al., FT-IR and FT-Raman study of hydrothermally degradated cellulose, J. Mol. Struct. 596 (2001) 163–169.
[73] B.G. Molina, et al., Smart design for a flexible, functionalized and electroresponsive hybrid platform based on poly(3,4-ethylenedioxythiophene) derivatives to improve cell viability, J. Mater. Chem. B 8 (2020) 8864–8877.
[74] S. Ali, Z. Khatri, K.W. Oh, I.S. Kim, S.H. Kim, Preparation and characterization of hybrid polycaprolactone/cellulose ultrafine fibers via electrospinning, Macromol. Res. 22 (2014) 562–568.
[75] Y.P. Yang, Y. Zhang, Y.X. Lang, M.H. Yu, Structural ATR-IR analysis of cellulose fibers prepared from a NaOH complex aqueous solution, IOP Conf. Ser. Mater. Sci. Eng. 213 (2017).
[76] A.C. Enache, I. Grecu, P. Samoila, C. Cojocaru, V. Harabagiu, Magnetic ionotropic hydrogels based on carboxymethyl cellulose for aqueous pollution mitigation, Gels 9 (2023) 358.

[77] Q. Chen, Y. Chen, C. Wu, Probing the evolutionary mechanism of the hydrogen bond network of cellulose nanofibrils using three DESs, Int. J. Biol. Macromol. 234 (2023) 123694.
[78] R.D. Abbott, D.L. Kaplan, Engineering biomaterials for enhanced tissue regeneration, Curr. Stem Cell Rep. 2 (2016) 140–146.
[79] H. Basri, et al., Mechanical degradation model of porous magnesium scaffolds under dynamic immersion, Proc. Inst. Mech. Eng. Part L J. Mater. Des. Appl. 234 (2020) 175–185.
[80] H. Zhang, L. Zhou, W. Zhang, Control of scaffold degradation in tissue engineering: a review, Tissue Eng. Part B Rev. 20 (2014) 492–502.
[81] S. Tajvar, A. Hadjizadeh, S.S. Samandari, Scaffold degradation in bone tissue engineering: an overview, Int. Biodeterior. Biodegrad. 180 (2023) 105599.
[82] Y. Gao, et al., Fabrication and characterization of collagen-based injectable and self-crosslinkable hydrogels for cell encapsulation, Colloids Surf. B. Biointerfaces 167 (2018) 448–456.
[83] V. Vatanpour, et al., Cellulose acetate in fabrication of polymeric membranes: a review, Chemosphere 295 (2022).
[84] J. Lee, A.A. Abdeen, T.H. Huang, K.A. Kilian, Controlling cell geometry on substrates of variable stiffness can tune the degree of osteogenesis in human mesenchymal stem cells, J. Mech. Behav. Biomed. Mater. 38 (2014) 209–218.
[85] G. Abagnale, et al., Surface topography enhances differentiation of mesenchymal stem cells towards osteogenic and adipogenic lineages, Biomaterials 61 (2015) 316–326.
[86] R. McBeath, D.M. Pirone, C.M. Nelson, K. Bhadriraju, C.S. Chen, Cell shape, cytoskeletal tension, and RhoA regulate stem cell lineage commitment, Dev. Cell 6 (2004) 483–495.
[87] C.E. Turner, Paxillin and focal adhesion signalling, Nat. Cell Biol. 2 (2000).
[88] C.H. Park, K.H. Kim, Y.M. Lee, W.V. Giannobile, Y.J. Seol, 3D printed, microgroove pattern-driven generation of oriented ligamentous architectures, Int. J. Mol. Sci. 18 (2017).
[89] B. Chen, C. Co, C.C. Ho, Cell shape dependent regulation of nuclear morphology, Biomaterials 67 (2015) 129–136.
[90] L. Yang, et al., Topography induced stiffness alteration of stem cells influences osteogenic differentiation, Biomater. Sci. 8 (2020) 2638–2652.
[91] S. Dupont, et al., Role of YAP/TAZ in mechanotransduction, Nature 4747350 (474) (2011) 179–183.
[92] G. Flamourakis, et al., Low-autofluorescence, transparent composite for multiphoton 3D printing, Opt. Mater. Express 11 (3) (2021) 801–813.
[93] K.I. Wada, K. Itoga, T. Okano, S. Yonemura, H. Sasaki, Hippo pathway regulation by cell morphology and stress fibers, Development 138 (2011) 3907–3914.
[94] C. Hsiao, et al., Human pluripotent stem cell culture density modulates YAP signaling, Biotechnol. J. 11 (2016) 662–675.
[95] Y. Hou, et al., Surface roughness gradients reveal topography-specific mechanosensitive responses in human mesenchymal stem cells, Small 16 (2020) 1905422.
[96] W. Yang, et al., Surface topography of hydroxyapatite promotes osteogenic differentiation of human bone marrow mesenchymal stem cells, Mater. Sci. Eng. C Mater. Biol. Appl. 60 (2016) 45–53.
[97] P.T. De Oliveira, S.F. Zalzal, K. Irie, A. Nanci, Early expression of bone matrix proteins in osteogenic cell cultures, J. Histochem. Cytochem. 51 (2003) 633–641.
[98] S. Vimalraj, Alkaline phosphatase: structure, expression and its function in bone mineralization, Gene 754 (2020).
[99] E.E. Golub, K. Boesze-Battaglia, The role of alkaline phosphatase in mineralization, Curr. Opin. Orthop. 18 (2007) 444–448.
[100] J. Sodek, et al., Regulation of osteopontin expression in osteoblasts, Ann. N. Y. Acad. Sci. 760 (1995) 223–241.
[101] M. Morinobu, et al., Osteopontin expression in osteoblasts and osteocytes during bone formation under mechanical stress in the calvarial suture in vivo, J. Bone Min. Res. 18 (2003) 1706–1715.
[102] M. Kenmotsu, K. Matsuzaka, E. Kokubu, T. Azuma, T. Inoue, Analysis of side population cells derived from dental pulp tissue, Int. Endod. J. 43 (2010) 1132–1142.
[103] B.W. Park, Y.S. Hah, D.R. Kim, J.R. Kim, J.H. Byun, Osteogenic phenotypes and mineralization of cultured human periosteal-derived cells, Arch. Oral Biol. 52 (2007) 983–989.
[104] H. Hanna, L.M. Mir, F.M. Andre, In vitro osteoblastic differentiation of mesenchymal stem cells generates cell layers with distinct properties, Stem Cell Res. Ther. 9 (2018).
[105] Y. Zhang, D. Li, Y. Liu, L. Peng, D. Lu, P. Wang, D. Ke, H. Yang, X. Zhu, C. Ruan, 3D-bioprinted anisotropic bicellular living hydrogels boost osteochondral regeneration via reconstruction of cartilage–bone interface, Innovation 5 (1) (2024) 100542.
[106] Q. Pang, Z. Chen, X. Li, J. Zhan, W. Huang, Y. Lei, W. Bao, Cytokine-activated mesenchymal-stem-cell-derived extracellular matrix facilitates cartilage repair by enhancing chondrocyte homeostasis and chondrogenesis of recruited stem cells, Research 8 (2025) 0700.
[107] L. Yang, W. Li, L. Shang, Y. Zhao, Macrophage-inspired magnetic silk fibroin porous microcarriers with exosome enrichment capability for bone repair, Chem. Eng. J. 520 (2025) 166322.
[108] B. Wang, L. Wang, T. Yuan, Y. Zhang, Q. Yang, H. Ou, B. Zhang, L. Yang, S. Li, Biomimetic microgrooved methacrylated silk fibroin cartilage scaffold for tracheal injury repair, Adv. Funct. Mater. (2025) e17195.
[109] L. Yang, X. He, W. Li, L. Shang, Bioinspired magnetic janus core–shell micromotors for delivery of stem cells and vascular endothelial growth factor in bone regeneration, Adv. Healthc. Mater. (2025) e01294.